ACS NANO
Cite This: ACS Nano 2018, 12, 11907−11916
www.acsnano.org

ARTICLE

Free Energy Landscape and Dynamics of Supercoiled DNA by High-Speed Atomic Force Microscopy

Tine Brouns,[†] Herlinde De Keersmaecker,[†] Sebastian F. Konrad,[‡] Noriyuki Kodera,[§] Toshio Ando,[§] Jan Lipfert,*[,‡] Steven De Feyter,*[,†] and Willem Vanderlinden*[,†,‡]

[†]KU Leuven, Division of Molecular Imaging and Photonics, Celestijnenlaan 200F, 3001 Leuven, Belgium

[‡]Department of Physics, Nanosystems Initiative Munich, and Center for NanoScience, LMU Munich, Amalienstrasse 54, 80799 Munich, Germany

[§]Nano-Life Science Institute (WPI-NanoLSI), Kanazawa University, Kakuma-machi, Kanazawa, 920-1192, Japan

Supporting Information

ABSTRACT: **DNA supercoiling fundamentally constrains and regulates the storage and use of genetic information. While the equilibrium properties of supercoiled DNA are relatively well understood, the dynamics of supercoils are much harder to probe. Here we use atomic force microscopy (AFM) imaging to demonstrate that positively supercoiled DNA plasmids, in contrast to their negatively supercoiled counterparts, preserve their plectonemic geometry upon adsorption under conditions that allow for dynamics and equilibration on the surface. Our results are in quantitative agreement with a physical polymer model for supercoiled plasmids that takes into account the known mechanical properties and torque-induced melting of DNA. We directly probe supercoil dynamics using high-speed AFM imaging with subsecond time and ∼nanometer spatial resolution. From our recordings we quantify self-diffusion, branch point flexibility, and slithering dynamics and demonstrate that reconfiguration of molecular extensions is predominantly governed by the bending flexibility of plectoneme arms. We expect that our methodology can be an asset to probe protein−DNA interactions and topochemical reactions on physiological relevant DNA length and supercoiling scales by high-resolution AFM imaging.**

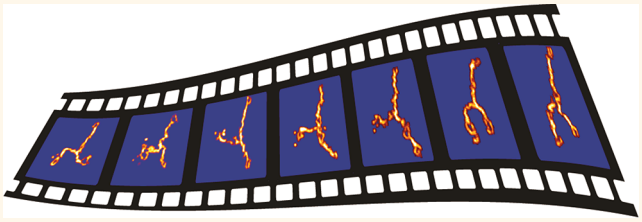

KEYWORDS: *DNA supercoiling, adsorption mechanisms, surface dynamics, energy landscape, atomic force microscopy*

DNA stores the genetic information in all cellular life. The readout and maintenance of DNA by processing enzymes is regulated by twisting and bending strains of the DNA helix. In the cell, DNA is organized in topological domains:[1,2] operational units of the genome wherein DNA twisting and bending deformations cannot change independently. This coupling of twisting and bending is described[3] by the theorem $Lk = Tw + Wr$ where the topologically invariant linking number Lk quantifies the number of chiral links between the double helix backbones, twist Tw is the total number of helical turns, and the writhing number Wr describes the bending of the double helix axis in three dimensions (Figure 1). DNA is supercoiled when Lk differs from the energetically most favorable value Lk_0 and the linking difference $\Delta Lk = Lk - Lk_0$ can be expressed in terms of deviations in twist ΔTw and writhe ΔWr from their equilibrium values ($\Delta Lk = \Delta Tw + \Delta Wr$). Twist deformations ΔTw affect formation of melting bubbles,[4] cruciform,[5] or Z-DNA[6] and can modulate protein binding.[7,8] Writing ΔWr occurs in the form of plectonemes, an interwound conformation of double-helical DNA, which enhances the target search of site-specific DNA-binding proteins[9] as well as protein-mediated loop formation.[10] Thus, organizing the genome in topological domains infers regulatory control over gene expression *via* DNA supercoiling. Consequently, the properties of DNA supercoiling have been intensively studied.

While structural and energetic properties of supercoiled DNA are relatively well understood from computer simulations and experiments,[11] the dynamics of DNA supercoils have been much less explored, in part due to the difficulties of simulating or measuring at the time and length scales involved. Experimental approaches to study supercoil dynamics involve magnetic[12−15] and optical tweezers[16,17] that can probe supercoiling-induced molecular extension changes with ∼nanometer (nm) spatial accuracy and ∼millisecond temporal

Received: September 12, 2018
Accepted: October 22, 2018
Published: October 22, 2018

DOI: 10.1021/acsnano.8b06994
ACS Nano 2018, 12, 11907−11916

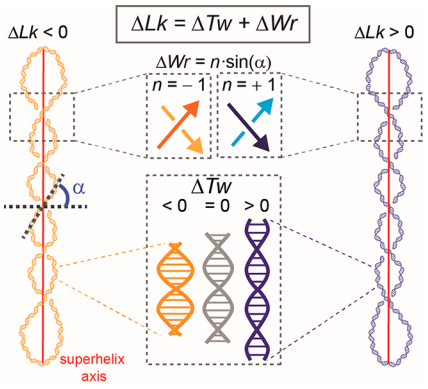

Figure 1. Relation between topological and geometrical parameters in supercoiled DNA. The linking difference ΔLk can be decomposed into deviations in twist ΔTw and writhe ΔWr. Negatively supercoiled DNA ($\Delta Lk < 0$, plasmid on the left) features n left-handed self-crossings, whereas positively supercoiled DNA ($\Delta Lk > 0$, plasmid on the right) features right-handed self-crossings. The writhing difference ΔWr can be written as the product of the number of self-crossings and the sine of the superhelix pitch angle α.[28] In negatively supercoiled plasmids, the twist difference ΔTw with respect to canonical B-DNA is negative, whereas ΔTw is positive in positively supercoiled plasmids. We note that DNA lengthens on overtwisting the double helix.[29−31]

resolution, by measuring end−end distances of individual molecules. While molecular tweezer approaches are powerful to resolve the overall end−end dynamics of plectonemic DNA, they do not resolve the local dynamics along the chain. Local structural dynamics of supercoils can be investigated using fluorescence microscopy.[18−20] Yet, the limited sensitivity of fluorescence microscopy is insufficient to detect small plectonemes, and the spatial resolution is limited by optical diffraction. In contrast, DNA structure can be sampled with ∼nm spatial resolution using electron or atomic force microscopy (AFM). AFM allows measuring molecules in a liquid environment but requires sufficiently stable adsorption on a solid support. Nevertheless, surface dynamics can be tuned by modifying the surface chemistry of the support. Lyubchenko,[21] Langowski,[22] and co-workers have demonstrated that local chain rearrangements can occur in negatively supercoiled DNA at the interface of aqueous buffer and aminosilane- or poly-lysine-modified mica. However, on surfaces that allow extensive DNA dynamics, negatively supercoiled ($\Delta Lk < 0$) plasmids exhibit only a minimal number of supercoil nodes.[23,24] It has been proposed that this effect arises from increased bending stress[25] or excluded volume effects on surface adsorption[26] or from generation of single-strand breaks catalyzed by the mica surface.[27] Irrespective of the underlying mechanism, the removal of negative plectonemic supercoiling on adsorption hinders the use of *in situ*, time-resolved AFM to study dynamics of plectonemes in negatively supercoiled plasmids and their interactions with proteins.

Here we demonstrate first that positively supercoiled plasmids ($\Delta Lk > 0$), in contrast to their negatively supercoiled counterparts ($\Delta Lk < 0$), maintain a plectonemic geometry on surfaces that favor surface equilibration at the molecular length scale and present an equilibrium model that quantitatively captures the observed geometries. We then use our protocol to visualize supercoil dynamics at the solid−liquid interface to quantify the rich dynamical behavior of positively supercoiled DNA at high spatiotemporal resolution and in a label-free fashion by high-speed AFM imaging. We show that under the conditions used supercoiled plasmids move as if they were in a quasi-2D solution, with a time scale for molecular reconfiguration on the order of ∼5 s. We conclude that our methodology can directly probe dynamics of supercoiled DNA, at bio-

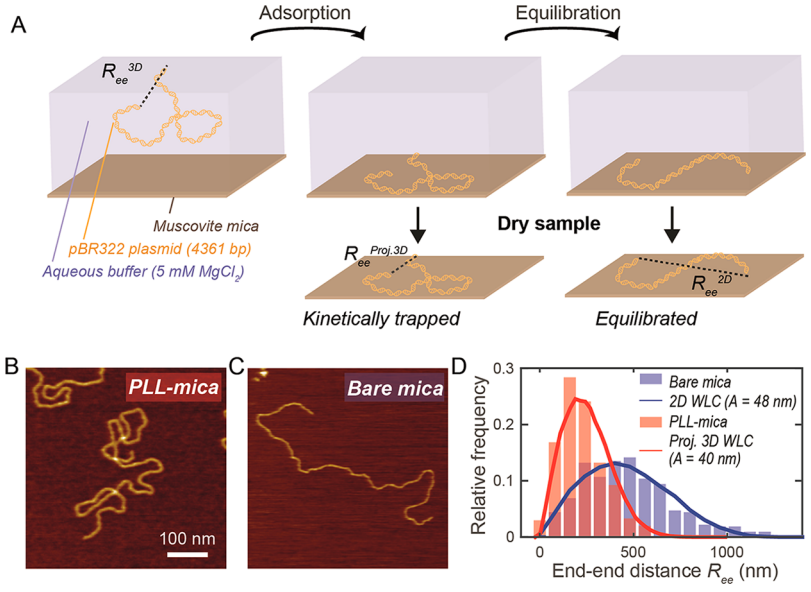

Figure 2. Kinetic trapping and equilibrium adsorption of linear pBR322 plasmids. (A) Schematic of adsorption mechanisms depicting kinetic trapping and surface equilibration. (B) AFM topograph of linear pBR322 adsorbed onto PLL-mica. (C) AFM topograph of linear pBR322 on bare mica. (D) End−end distance distribution for linear pBR322 adsorbed on bare mica (blue bars) is well reproduced by the end−end distribution of 10^5 simulated 2D worm-like chain molecules with bending persistence length A = 48 nm (blue line; χ^2_{Red} = 0.84).[40] The end−end distance histogram of linear pBR322 on PLL-mica (red bars) closely resembles the distribution of 2D-projected end−end distances of 10^5 simulated 3D worm-like chain molecules with A = 40 nm (red line; χ^2_{Red} = 1.24).

DOI: 10.1021/acsnano.8b06994
ACS Nano 2018, 12, 11907−11916

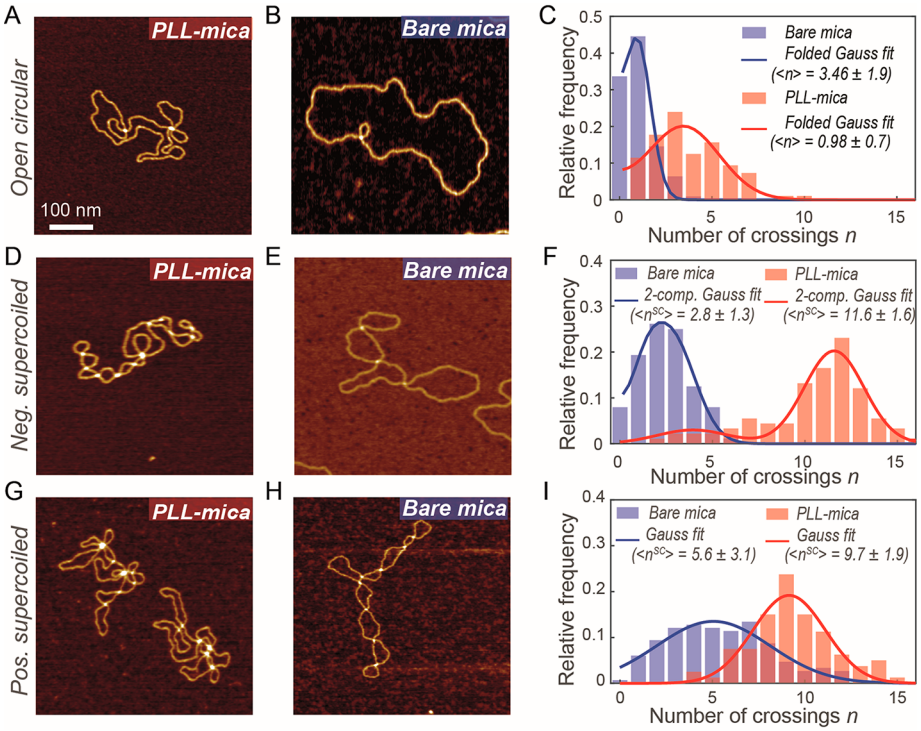

Figure 3. Kinetic trapping and equilibrium adsorption of circular pBR322 plasmids. (A) AFM topograph of open circular pBR322 on PLL-mica. (B) Topograph of open circular pBR322 on bare mica. (C) Distributions of the number of self-crossings per molecule *n* for open circular pBR322 on bare mica (blue bars) and PLL-mica (red bars) and fits with a folded Gaussian function (solid lines). (D) Topographic image of negatively supercoiled pBR322 on PLL-mica. (E) Topograph of negatively supercoiled pBR322 on bare mica. (F) Distributions of the number of self-crossings *n* for negatively supercoiled pBR322 on bare mica (blue bars) and PLL-mica (red bars) and fits to a two-component Gaussian distribution (lines). The distribution at lower *n* values corresponds to open circular plasmids, and the mean and standard deviation were fixed at the values found through fitting the distributions shown in (C). (G) Topograph of positively supercoiled pBR322 on PLL-mica. (H) Topograph of positively supercoiled pBR322 on bare mica. (I) Distributions of the number of self-crossings *n* for positively supercoiled pBR322 on bare mica (blue bars) and PLL-mica (red bars) and fits to a single Gaussian distribution.

logically important length and time scales that hitherto have remained elusive.

RESULTS

Kinetic Trapping and Surface Equilibration Adsorption at the Molecular Scale. In general, adsorption strongly affects the geometry of long semiflexible polymers such as DNA. We distinguish two extreme cases[32] (Figure 2A): The first case, termed kinetic trapping, occurs when surface interactions are strong and friction on the surface is very large, such that the molecule does not undergo conformational reconfiguration and does not equilibrate on the surface after adsorption. In the other limiting case, called surface equilibration, interactions with the surface are weak enough that the molecule remains mobile and can equilibrate in 2D. Under conditions that allow for surface equilibration, molecules adopt configurations that correspond to equilibrium configurations in 2D and that are governed by the intrinsic elastic properties and excluded volume effects of the molecule. To directly probe the extent of surface equilibration under different deposition conditions, we used AFM imaging of dried samples to investigate the geometry of linearized pBR322 plasmid DNA (4361 bp) on different surfaces.

In a first set of experiments, linearized pBR322 was adsorbed either onto freshly cleaved bare mica (N = 304 imaged molecules) or on mica modified with poly-L-lysine (PLL-mica) (N = 319 imaged molecules) from an aqueous buffer with 5 mM $MgCl_2$ (Figure 2). DNA contour lengths were measured by automated tracing of chains[33] with a step length of l = 5 nm and correspond to an average rise per bp of 0.325 ± 0.01 nm, in excellent agreement with other solution-based measurements, such as FRET[34] and small-angle X-ray scattering interference,[35,36] on B-form DNA (Figure S1). To evaluate the global chain conformation, we quantified the overall end−end distance, R_{ee}, for each of the imaged molecules. We then compared the distribution of end−end distances from the molecular ensemble with predictions from the worm-like chain (WLC) model that treats DNA as a continuous polymer with a bending persistence length A. Molecules adsorbed onto PLL-mica appear "entangled" and relatively compact (Figure 2B), and the R_{ee} distribution is accurately described (χ^2_{Red} = 1.24) by a 2D-projected 3D WLC model with bending persistence length A = 40 nm (Figure 2D), in good agreement with solution values for A in the presence of Mg^{2+}.[37] An alternative model for kinetic trapping proposes that the end−end distance of the chain in 3D is preserved on adsorption.[38,39] Our experimental data do not support this model, at least at the global length scale of the molecule: Fitting the experimental data to the 3D end−end distance distribution of simulated chains, we find a poorer fit (χ^2_{Red} = 2.17) than for the 2D-projected 3D WLC model and an unrealistically small value of A = 22 nm (Table S1).

On bare mica DNA is more extended (Figure 2C) and a 2D WLC model with A = 48 nm describes the distribution best (Figure 2D, Table S1; χ^2_{Red} = 0.84). The excellent fit of the 2D WLC model to the bare mica data suggests that the molecules

DOI: 10.1021/acsnano.8b06994
ACS Nano 2018, 12, 11907−11916

assume equilibrium conformations at the surface. The larger value for A in 2D might follow from self-avoidance, an effect not included in our chain simulations, but that would play a larger role in 2D than in 3D. We conclude that at the global length scale, DNA adsorbs on PLL-mica in a kinetically trapped conformation, while on bare mica the chains equilibrate at the solid−liquid interface.

Geometry of Kinetically Trapped and Surface-Equilibrated Circular Plasmids. Next, we evaluated the geometry of plasmids with a circular topology that are not torsionally constrained (open circular; Figure 3A−C). We generated open circular plasmids by introducing a single nick in the DNA backbone through incubation with the nicking enzyme Nt.BspQI (see Methods) and quantified their geometry by counting the number of crossovers n per molecule for plasmids adsorbed on PLL-mica and on bare mica. Molecules adsorbed on PLL-mica (N = 96) feature frequent self-crossings (Figure 3A). The node number distribution, *i.e.*, the number of self-crossings, is well-described by a folded Gaussian with n = 3.46 ± 1.9 (mean ± SD; Figure 3C). In contrast, on bare mica, open circular pBR322 (N = 110) exhibit few self-crossings (Figure 3B) and the node number distribution is well-described by a folded Gaussian with n = 0.98 ± 0.7 (mean ± SD; Figure 3C). Therefore, our data demonstrate that surface equilibration involves partial removal of loops trapped on initial adsorption.

In supercoiled circular DNA, both bending and twisting degrees of freedom contribute to the energy of the system. To understand the effect of supercoiling chirality on the geometry of molecules adsorbed under conditions of kinetic trapping (PLL-mica) and equilibrium adsorption (bare mica),[41] we generated positively supercoiled plasmids using the archaeal protein rHMfB and topoisomerase Ib (Figure S2).[42] We use the band counting method to quantify the linking difference ΔLk of the supercoiled molecules separated by gel electrophoresis,[43] with respect to plasmids relaxed in buffer used for AFM sample deposition. To ensure a narrow distribution of topoisomers for AFM experiments, we purified DNA with $\langle \Delta Lk \rangle \approx +10 \pm 3$ (mean ± SD; corresponding to $\sigma = +0.024$; Figure S2) by preparative gel electrophoresis. We used a commercially available, negatively supercoiled pBR322 sample with similar supercoiling density (mean ± SD; $\langle \Delta Lk \rangle = -12 \pm 2$; $\sigma = -0.029$) to compare the effect of supercoil chirality on the geometry of surface-adsorbed plasmids.

Kinetic Trapping on PLL-Mica Probes the Partitioning of Linking Number in Solution. On PLL-mica, both positively and negatively supercoiled plasmids adopt a plectonemic geometry and exhibit significantly more self-crossings than the open circular constructs under the same conditions (Figure 3D,G). For negatively supercoiled plasmids (N = 92) the node number distribution has a major peak at n = 11.6 ± 1.6 (~85% of molecules) and a minor population at n = 3.5 ± 1.9 (~15%), which we attribute to a small fraction of nicked molecules in the commercial plasmid sample (Figure 3F). For positively supercoiled pBR322 adsorbed on PLL-mica (N = 82), the node number distribution features a single peak centered at n = 9.7 ± 1.9 (mean ± SD; Figure 3I). There are only very few molecules (<5%) in the range of self-crossing expected for open circular plasmids under these conditions, confirming the successful and damage-free purification of highly positively supercoiled DNA from agarose gels in our protocol.

The number of self-crossing n quantified from AFM images can be related to ΔWr *via* $|\Delta Wr| = n \sin \alpha$ with α being the superhelix pitch angle (Figure 1).[28] From quantification of our AFM images, we find $\alpha = 53 \pm 15°$ and $\alpha = 52 \pm 10°$ (mean ± SD) for negative and positive supercoiling, respectively, in excellent agreement with previous results.[22,44] We calculate $\Delta Wr = -9.3 \pm 2.2$ (mean ± SD) for the negatively supercoiled sample and $\Delta Wr = 7.6 \pm 1.8$ (mean ± SD) for the positively supercoiled sample. In turn, the value of ΔWr can be compared to the distributions of topoisomers with linking differences ΔLk present in the plasmid samples that were obtained from band counting of topoisomer distributions separated by gel electrophoresis (Figure S2).[43] With $\Delta Lk = -12 \pm 2$ and $+10 \pm 3$ (mean ± SD) (corresponding to $\sigma = \Delta Lk/\Delta Lk_0 = -0.029 \pm 0.005$ and $+0.024 \pm 0.007$) we can quantify the partitioning of the linking number as $\Delta Wr/\Delta Lk \approx 0.77 \pm 0.04$ and $\sim 0.76 \pm 0.05$ (mean ± SEM) for negatively and positively supercoiled plasmids, respectively. The measured values for $\Delta Wr/\Delta Lk$ suggest that irrespective of the sign of the supercoiling three-fourths of the total linking difference partitions into writhe, in excellent agreement with previous results for negatively supercoiled plasmids.[45−47] These results confirm that supercoiled DNA adsorbed on PLL-mica probes the solution-phase plectoneme geometry and preserves the torque stored in the DNA on adsorption.[7] In addition, the results suggest that the partitioning between Tw and Wr in solution does not depend on the sign of supercoiling, at least for the range of values probed.

The Asymmetric Torsional Response of DNA Explains Distinctive Geometries of Positively and Negatively Supercoiled Plasmids upon Surface Equilibration on Bare Mica. On bare mica, negatively supercoiled plasmids lose the characteristic plectonemic geometry and exhibit very few self-crossings (Figure 3E, Figure S3). The node number distribution (N = 93) was fitted using a two-component Gaussian distribution, reflecting the open circular and supercoiled fraction (Figure 3F). We constrained the fit by fixing the parameters of the open circular fraction ($\langle n^{OC} \rangle$ = 0.98 ± 0.7; Figure 2F) and find $\langle n^{SC} \rangle$ = 2.8 ± 1.3 for the supercoiled fraction, in qualitative agreement with previous reports.[24,27,48] The superhelix angle was measured as $\alpha = 47 \pm 18°$, resulting in $\Delta Wr = -n \sin \alpha = -2.0 \pm 1.4$. In contrast, positively supercoiled pBR322 plasmids maintain a plectonemic geometry (Figure 3H), in qualitative agreement with a recent report,[41] for which the node number distribution (Figure 3I) can be described using a single Gaussian distribution with n = 5.6 ± 3.1 (N = 149). The superhelix pitch angle (Figure 1) was found to be $\alpha = 51 \pm 16°$, yielding ΔWr = 4.4 ± 2.6. Thus, on a surface that allows large-scale surface dynamics, supercoiled plasmids exhibit fewer self-crossings as compared to the kinetically trapped situation, and this loss of plectonemes is more severe for negatively *versus* positively supercoiled DNA.

To understand the pronounced effect of supercoil chirality on the observed geometries of equilibrated supercoiled DNA, we calculate the supercoiling energy ΔG_{SC} as the sum of the free energies of writhing ΔG_{Wr} and twisting ΔG_{Tw} of the DNA double helix ($\Delta G_{SC} = \Delta G_{Wr} + \Delta G_{Tw}$). Compared to supercoiling in 3D, writhing in 2D is unfavorable for two reasons: First, the DNA bending persistence length[49] increases with reduced dimensionality d: ($A \propto 2/(d-1)$). We use an analytical expression to estimate the bending energy ΔG_{bend} in a plectoneme (see Methods).[47] In addition, plectonemes

DOI: 10.1021/acsnano.8b06994
ACS Nano 2018, 12, 11907−11916

feature crossovers that are unfavorable in (quasi-)2D because of excluded volume effects.[26,50,51] The energy penalty for excluded volume effects can be written as $\Delta G_{Excl} = n\Delta G_1 = Wr/\sin\alpha\ \Delta G_1$ with ΔG_1 being the energetic penalty per crossover (Figure 4A). The writhing free energy thus includes

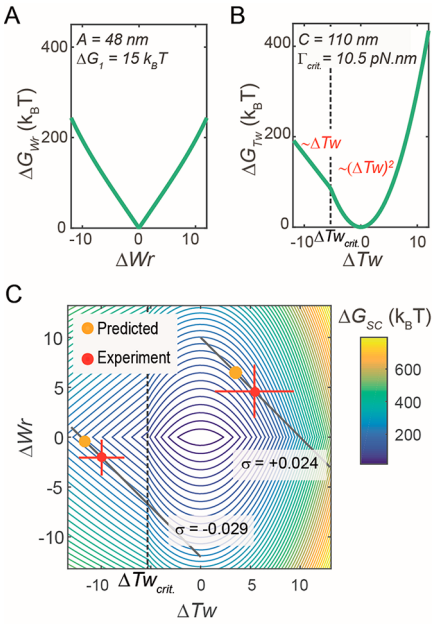

Figure 4. An equilibrium elasticity model captures the effect of supercoil chirality on the surface geometry in supercoiled plasmids. (A) Writhing free energy ΔG_{Wr} as a function of ΔWr considering bending strain in the plectoneme with A = 48 nm and excluded volume effects by electrostatic repulsion at chain crossovers, with energy penalty per crossing as free parameter (here $\Delta G_1 = 15 k_BT$). (B) Twisting free energy ΔG_{Tw} as a function of ΔTw with torsional stiffness C = 110 nm, and critical torque Γ_{crit} = −10.5 pN·nm corresponding to critical twist difference ΔTw_{crit} = 5.3. For $\Delta Tw > \Delta Tw_{crit}$, ΔG_{Tw} scales with $(\Delta Tw)^2$, while for $\Delta Tw < \Delta Tw_{crit}$, ΔG_{Tw} is linear in ΔTw. (C) Two-dimensional ΔG^{SC} energy landscape along ΔWr and ΔTw degrees of freedom, for surface-equilibrated supercoiled pBR322. Topological constraints limit the conformational space, and lines of constant supercoiling density are shown (black lines) for σ = −0.029 and σ = +0.024. Orange points denote predicted minimum energy conformation; red points denote experimental data ($\langle\Delta Wr\rangle \pm$ SD; $\langle\Delta Tw\rangle \pm$ SD).

bending strain and excluded volume effects ($\Delta G_{Wr} = \Delta G_{bend} + \Delta G_{excl}$), which both increase on adsorption and favor plectoneme removal upon equilibrium adsorption. In topologically constrained DNA, the energy involved in writhing is balanced by the torsional energy due to twisting. The (intrinsic) twist persistence length[11,52] $C \approx 110$ nm is unaffected by reduction of dimensionality,[53,54] and the twist energy is approximated by $\Delta G_{Tw} = Ck_BT/L(2\pi\Delta Tw)^2$. However, this harmonic approximation is only valid within a certain range of ΔTw: for negatively supercoiled, *i.e.*, underwound DNA, the harmonic regime breaks down at a critical torque[11,52,55] of $\Gamma_{crit} = -10.5 \pm 1$ pN·nm (corresponding to an excess twist $\Delta Tw_{crit} = -5.3$ for pBR322), where it becomes energetically favorable for the double-helix to melt. For $\Delta Tw < \Delta Tw_{crit}$, the torque remains constant at $\Gamma_{crit.}$ and ΔG_{Tw} increases linearly with ΔTw (Figure 4B). In contrast, ΔG_{Tw} increases quadratically on overtwisting the double helix (at least up to a torque of $\Gamma = +35 \pm 1$ pN·nm, where the transition of B-DNA to P-DNA[11,52] occurs, corresponding to an excess twist $\Delta Tw \geq 18$, *i.e.*, beyond the range of ΔTw relevant to our measurements).

We construct a two-dimensional energy landscape by plotting the supercoiling energy along both the writhe and twist degrees of freedom (Figure 4C). To optimize the energy landscape with respect to our experimental data, we vary ΔG_1 while keeping the other parameters fixed at accepted literature values (see above). With ΔG_1 as the only adjustable parameter, we obtain an excellent description of the data for $\Delta G_1 = 15 \pm 1$ k_BT. The experimental results for both positively and negatively supercoiled plasmids are within experimental errors of the predicted free energy minima in the (ΔTw, ΔWr) free energy landscape (Figure 4C). Our model correctly captures the pronounced asymmetry between negative and positive supercoiling: It predicts that upon equilibration at the surface, the linking number for negatively supercoiled plasmids is almost completely absorbed by twist such that $\Delta Tw \approx \Delta Lk$ and $\Delta Wr \approx 0$, mostly due to DNA melting. In contrast, for positively supercoiled plasmids, ΔLk partitions approximately equally between ΔTw and ΔWr.

Surface Dynamics of Equilibrated Positively Supercoiled Plasmids on Bare Mica by High-Speed AFM. Equilibration after adsorption implies that the molecules can undergo conformational dynamics at the surface, and we aimed to investigate whether dynamics of equilibrated positively supercoiled plasmids can be imaged in real time using *in situ* AFM. Exploiting the capabilities of high-speed AFM to sample biomolecular dynamics at subsecond frame rates while being minimally intrusive,[56] we found that supercoiled DNA exhibits extensive dynamics at the interface of bare mica and an aqueous buffer comprising 5 mM Mg^{2+} ions (Figure 5A, Supplementary Movie 1). We recorded movies (minimally 200 frames) of individual supercoiled molecules with 2.5 nm and 600 ms spatiotemporal resolution and used quantitative approaches to evaluate the time scales and flexibility of different dynamic modes.

First, we quantify molecular self-diffusion of entire plasmids: for each topographic image, the 2D -projected center of mass r_{cm} was determined (Figure 5B). The time-averaged mean-squared displacement $\langle MSD(t)\rangle$ is consistent with a subdiffusive model in all cases (Figure 5C), and fitting to $\langle MSD(t)\rangle = 4Dt^{\alpha}$ yields a self-diffusion coefficient $D_{self} = 24 \pm 8$ nm^2/s and scaling exponent $\alpha = 0.6 \pm 0.1$ (error is SD; $n_{molecules} = 7$). Subdiffusion and variability in D_{self} might follow from spatial heterogeneity of DNA-binding energies on the mica surface.[57] To assess conformational flexibility and dynamics of supercoiled plasmids, we quantify the overall size of the molecule by computing the radius of gyration R_g for each subsequent image in movies of supercoiled plasmids (Figure 5D). Over all conformations (n = 2314; $n_{molecules} = 7$) $R_g^{2D} = 55 \pm 8$ nm (error is SD). In addition, we compute the autocorrelation function and estimate the correlation time τ_{Rg} from a single-exponential fit (Figure 5E). We find $\tau_{Rg} \approx 3.9 \pm 1.1$ s (error is SD; $n_{molecules} = 7$), indicating relatively rapid conformational dynamics.

Our data depict supercoiled DNA plasmids predominantly in branched plectoneme geometries. Branching increases the number of possible molecular conformations and enriches molecular dynamics.[45,58] In turn, it has been predicted that supercoil branching results in a dramatic increase of the rate of protein-mediated intramolecular reactions.[59] We identified

DOI: 10.1021/acsnano.8b06994
ACS Nano 2018, 12, 11907−11916

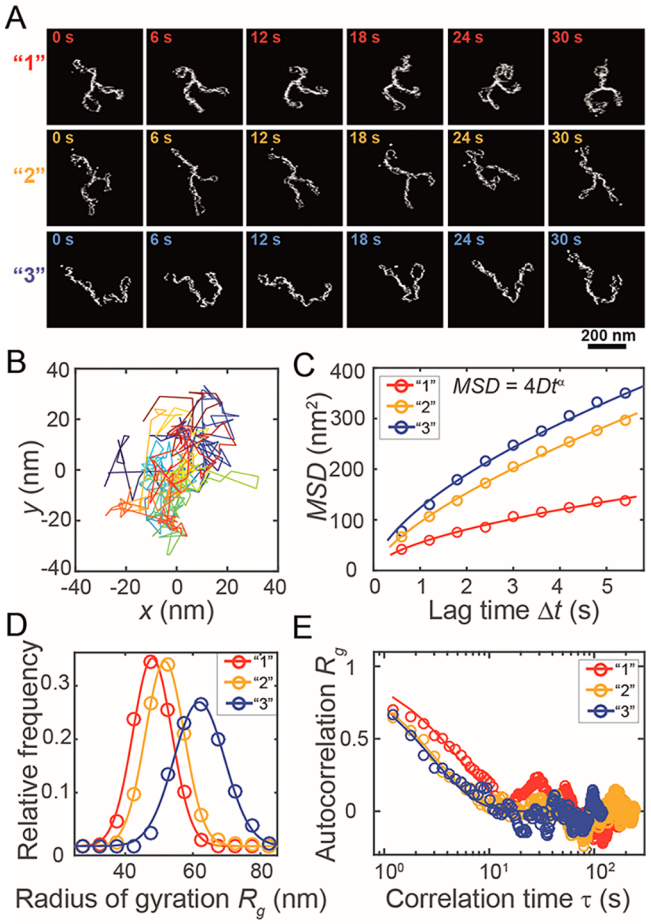

Figure 5. Molecular dynamics of surface-equilibrated positively supercoiled pBR322 plasmids. (A) Sequences of time-resolved molecular conformations of supercoiled plasmids for three different molecules ("1", "2", and "3"). The images are background-subtracted. (B) Plot of the center of mass of molecule "2" as a function of time; time is color-coded from blue to red. (C) Mean square displacement of the center of mass as a function of lag time and fits to a subdiffusion model. Color code same as in (A). (D) Plot of radius of gyration as a function of time for molecules "1", "2", and "3". (E) Normalized autocorrelation of R_g as a function of correlation time τ, and single exponential fits to the data.

how flexible features in branched plectonemes contribute to conformational dynamics observed globally *via* the correlation time τ_{Rg}. First, we quantify changes in length l_i of the plectoneme arms (Figure 6A) by measuring the fractional volume of each arm in consecutive frames and converting these values to the respective arm lengths l_i. The individual arm length distributions are normally distributed, indicative of a diffusion mechanism (Figure 6B). The time-averaged MSDs of the arm lengths are well-described by a subdiffusion model. At the level of individual plectoneme branches, we find diffusion coefficients $D_{Rept} = (4.4 \pm 1.1) \times 10^2$ nm^2/s and scaling exponents $\alpha = 0.35 \pm 0.12$ (Figure 6C). The data suggest that the diffusion of the arms on short time scales is faster than the diffusion of the entire molecule on the surface, suggesting that local, intramolecular dynamics are initially faster than global diffusion. However, the MSD for the diffusion of the arms grows with a smaller scaling exponent, suggesting that the intramolecular dynamics are constrained by internal processes.

Next, we quantify the interarm angles ϕ_i by connecting the center of the supercoil branching point with the first crossover in each arm (Figure 6D) and find distributions of all interarm angles to be normally distributed (Figure 6E). The widths of the distributions are broad, with SD(ϕ) ≈ 20°, implying a flexible branching point. To quantify the time scale for branch point dynamics, we calculated the autocorrelation of ϕ_i (Figure 6F). An exponential fit to the data yields correlation times $\tau \approx$ 1−2 s. Despite these fast dynamics, changes of ϕ_i do not correlate significantly with changes in R_g, implying that branch point flexibility does not govern global reconfiguration of molecular extension.

Last, we quantify plectoneme bending flexibility and dynamics. To this end we discretize plectoneme axes between the branch point and the midpoint of plectoneme end-loops (Figure 6G). Bending flexibility of plectonemes is then measured in terms of the dependence of squared end−end distances r^2 of the plectoneme, on the axis length λ. In analogy with the flexibility of a single polymer chain, one can fit the data to a 2D worm-like chain model. While quantification by the WLC model can provide only a rough approximation for plectoneme bending persistence, it is satisfactory to find a plectoneme bending persistence length $A_{plect} = 76 \pm 9$ nm that is twice the persistence length of double-stranded DNA (A = 40 nm; see Figure 2) under the same conditions, as expected for two dsDNA chains that are in first approximation aligned in a parallel fashion (Figure 6H). Plectoneme bending dynamics was quantified by calculating the autocorrelation of r^2/λ, and fitting with a single exponential yields a correlation time $\tau = 6 \pm 1$ s (Figure 6I).

In addition, we evaluated how combined changes in plectoneme arm bending correlates with changes in molecular radius of gyration. We find a Pearson's correlation coefficient PCC = 0.55, indicating that the bending dynamics of plectoneme arms governs the time scale of molecular extension reconfiguration to a large extent, in agreement with a theoretical prediction.[59]

CONCLUSION

DNA supercoiling constrains the kinetics of nuclear processes such as replication, transcription, and recombination. Appreciating how supercoiling controls such processes requires a thorough understanding of supercoil dynamics. Here we show how atomic force microscopy can capture supercoil dynamics in real time, identifies flexible features in supercoiled plasmids, and quantifies the time scales of supercoil dynamics at submolecular level. In particular, we have demonstrated that supercoil branching points are flexible and highly dynamic and that the bending dynamics of plectonemes governs the overall molecular relaxation time. In addition, quantification of the size fluctuations of plectoneme arms demonstrated that diffusion of DNA monomers by slithering along the chain contour is well-described by a subdiffusion model with exponent $\alpha \approx 0.35$. It is tempting to speculate on the molecular mechanisms underlying this subdiffusive behavior. While the theory for reptation of monomers in a linear chain[51] suggests a scaling exponent $\alpha = 1/2$, it is unclear how reptation along a branching point in a branched supercoil would affect scaling. Recently, Jia and Muthukumar[60] have reported that a combination of conformational entropy and local chain dynamics, which are frustrated by topological confinement, yields a scaling exponent $\alpha = 1/3$. Future high-speed AFM experiments using positively supercoiled plasmids of different

DOI: 10.1021/acsnano.8b06994
ACS Nano 2018, 12, 11907−11916

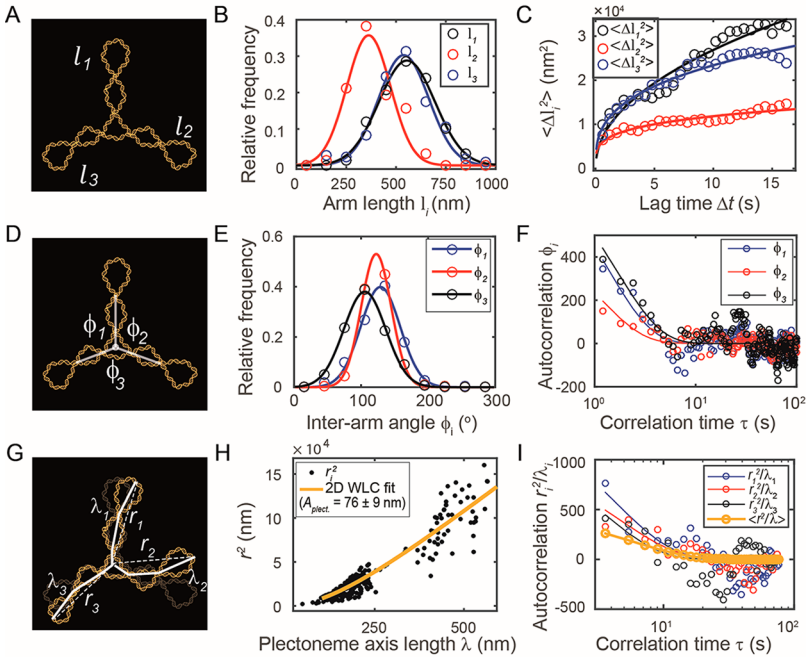

Figure 6. Flexibility and time scale of dynamic elements in branched supercoiled plasmids. (A) The length l_i of plectoneme arms in branched supercoils changes over time *via* slithering dynamics over the branch point. (B) Arm length distributions for a single branched supercoiled plasmid. Data are fit with a Gaussian distribution. (C) Mean-squared changes in arm length $\langle \Delta l_i^2 \rangle$ as a function of lag time Δt and fit to a subdiffusion model. (D) Scheme depicting the interarm angles centered at the branch point. (E) Interarm angle distributions for a single branched supercoiled plasmid and fits to Gaussian distributions. (F) Autocorrelation of interarm angles and fits with a single-exponential function. (G) Scheme depicting bending flexibility of plectonemes, with λ_i being the length of the plectoneme axis and r_i the end−end distance of the plectoneme. (H) Dependence of the squared end−end distance of plectonemes on plectoneme axis length, fitted to a 2D WLC model with A_{plect} = 76 ± 9 nm. (I) Autocorrelation of r_i^2/λ_i^2 and fits to single exponentials, with correlation times τ = 6 ± 1 s.

length, as well as on alternative surfaces (*e.g.*, supported lipid bilayers[61,62]), could help us understand the molecular mechanisms underlying the scaling behavior observed in this work.

Evidently, adsorption onto a solid support as required for imaging of molecular conformations by AFM infers increased friction that affects the time scales of molecular dynamics. Therefore, it is of interest to compare our results obtained in quasi-2D with those obtained for supercoiled plasmids in 3D. Self-diffusion of supercoiled pBR322 in free solution[63] is characterized by a diffusion coefficient of ~3.8×10^{-12} m^2 s^{-1}, approximately 5 orders of magnitude faster as compared to our measurements of $D_{self} \approx 2.5 \times 10^{-17}$ m^2 s^{-1} at the interface of bare mica and a Mg^{2+}-containing aqueous buffer. Autocorrelation of the radius of gyration presents a means to investigate internal conformational dynamics at the global scale and has previously been used by Vologodskii and co-workers to evaluate supercoil dynamics *in silico*.[64] While radius of gyration correlation times were only calculated for supercoiled plasmids up to 3000 bp in length, extrapolation to 4631 bp for pBR322 would result in a time scale of ~$(1-2) \times 10^{-4}$ s, or ~4 orders of magnitude faster in comparison to the time scale of conformational dynamics observed in 2D on mica. Langowski and co-workers used dynamic light scattering[63] at high scattering vectors to estimate the diffusion constant for internal reptation in free solution to be ~15×10^{-12} m^2 s^{-1}, approximately 4 orders of magnitude faster as compared to the value we measured on the mica surface ($D_{Rept} = (4.4 \pm 1.1) \times 10^{-16}$ m^2 s^{-1}). We conclude that surface dynamics are much slower as compared to supercoil mobility in 3D solution. Nevertheless, we find that the different dynamic modes are slowed down to a similar extent with respect to the situation in free solution, implying that dynamics occurs in a quasi-2D solution. In addition, our time-resolved data indicate that conformational reconfiguration occurs at the ~seconds time scale. This time scale is easily accessible using high-speed AFM and is within the range typically associated with protein−DNA association times. We therefore anticipate that the methodology presented here will serve to study interaction pathways of DNA-binding proteins and DNA topochemical enzymatics by direct visualization at the ~nm scale.

METHODS

DNA Substrates and Reagents. Negatively supercoiled pBR322 plasmid (4361 bp), T5 exonuclease, and the Monarch DNA gel extraction kit were purchased from NEB (Ipswitch, MA, USA). Wheat germ topoisomerase I was purchased from Inspiralis (Norwich, UK). SYBR gold was purchased from Invitrogen (Thermo Fisher Scientific, Waltham, MA, USA). All other chemical products were purchased from Sigma-Aldrich (St. Louis, MO, USA).

Preparation of Positively Supercoiled DNA. Positively supercoiled DNA was prepared as described before,[42] with minor modifications. Relaxed pBR322 was prepared by treatment of commercial negatively supercoiled DNA with wheat germ topoisomerase I. The reaction product was purified *via* phenol/chloroform/isoamyl alcohol extraction followed by ethanol precipitation. The final DNA was immediately resuspended in 1× rHMfB reaction buffer (10 mM Tris, 4 mM EDTA, 8 mM K_2HPO_4, 200 mM NaCl, pH 8.0). A 0.5 μg amount of relaxed DNA (20 μg/mL final concentration) was then incubated with the optimal proportion of archaeal histone rHMfB, which was in our study a protein-to-DNA ratio of ~0.5 (Figure S2). In 1× rHMfB buffer, with low ionic strength, topologically relaxed plasmids will bind to tetramers of rHMfB, which constrains the DNA in a positively supercoiled toroidal

DOI: 10.1021/acsnano.8b06994
ACS Nano 2018, 12, 11907−11916

geometry. Compensatory, negatively supercoiled plectonemes are formed in the unbound portion of the plasmid. These plectonemes were removed by adding 1.5U wheat germ topoisomerase I, following adjustment of the buffer by addition of a 1/10 volume of reaction buffer II (590 mM Tris, 8 mM K_2HPO_4, 22 mM EDTA, 100 mM NaCl, pH 8.0) and addition of a 1/10 volume of water. This reaction was incubated for 1.5 h at 37 °C. The DNA was purified further, and the archaeal protein was removed *via* phenol/chloroform/isoamyl alcohol extraction followed by ethanol precipitation, resulting in plasmids with positive supercoiling. This process was repeated twice to increase the degree of supercoiling (Figure S2).

Agarose Gel Electrophoresis. To determine superhelical density, agarose gel electrophoresis was used. To differentiate between topoisomers with different levels of DNA supercoiling, we also performed gel electrophoresis (1% agarose) in electrophoresis buffers containing 5 mM $CaCl_2$ or 1.5 μM chloroquine. Electrophoresis was performed in horizontal slab gels submerged in Tris-acetate-EDTA buffer. The electrophoresis was carried out at 5 V/cm for 4 h at 4 °C. After electrophoresis, gels were stained with SYBR Gold (0.5×). Images were taken with a Gel Doc XR+ system.

Gel Extraction. To ensure a narrow distribution of topoisomers in our experiments, only the plasmids with the highest degree of supercoiling were gel extracted by use of the Monarch DNA gel extraction kit. To remove all nicked molecules generated during the process of gel extraction, the extracted DNA was subsequently treated with T5 exonuclease. The protein was removed, and the DNA was purified *via* phenol/chloroform extraction followed by ethanol precipitation.

AFM Imaging in Air. For imaging in air and under kinetic trapping conditions, the plasmids (0.5 ng/μL) were drop-casted onto poly-L-lysine-coated (0.01%) mica from deposition buffer (10 mM Tris-HCl, 5 mM Mg-acetate; pH = 8) for 30 s, rinsed with milli-Q water (30 mL), and dried using a gentle stream of Ar gas. For imaging in air and under surface equilibration conditions, the plasmids (0.35 ng/μL) were deposited onto mica in deposition buffer for 5 min, rinsed with Milli-Q water (30 mL), and gently dried using Ar gas. AFM images were collected using a Multimode VIII AFM (Bruker) operated in tapping mode. Silicon tips (AC160TS, drive frequency of 300−350 kHz, Olympus) were used. AFM images of 2 × 2 μm^2 were recorded with 2048 × 2048 pixels at a scanning speed of 2 Hz. All AFM acquisitions were performed at room temperature.

AFM Imaging in Liquid. All HS-AFM observations were performed on a custom-built high-speed AFM described previously.[65] For HS-AFM observations, DNA samples were diluted in imaging buffer (10 mM $MgCl_2$, 10 mM Tris, pH 7.4) to a final concentration of 0.35 ng/μL. Subsequently, 2 μL of the sample was deposited for 5 min on a freshly cleaved mica disk with a diameter of 1.5 mm. The liquid cell was gently washed three times with imaging buffer (~60 μL). Next, the liquid cell was filled with imaging buffer to perform HS-AFM observations at room temperature. An AC10 cantilever tip (Olympus, Tokyo) was modified by electron-beam deposition and subsequent argon-plasma sharpening. When a target molecule was found, imaging parameters (cantilever oscillation amplitude, excitation frequency, and set point voltage) were readjusted until high-resolution images appeared.

AFM Image Analysis. Processing and analysis of AFM images recorded on dried samples involved the use of a commercial scanning probe image processor (SPIP v6.3.5; Image Metrology). Images were flattened using a line-wise correction with a polynomial fit. End−end distances of linear chains were determined using the Caliper tool. Contour length measurements were performed using a previously published algorithm[33] that traces digital images of linear molecules by discretizing the chain using step sizes of 5 nm. To stringently test the adsorption mechanism of chains deposited on bare mica or PLL-mica, we simulated chains of 4361 base-pairs and varied the bending persistence length A. For each simulation, we determined the end-to-end distances R_{ee} of 10^5 chains and calculated the reduced χ^2 value for different models (*i.e.*, 2D WLC, 2D-projected 3D WLC, 3D WLC) to achieve the best fit to the experimental data. For circular plasmids, we quantify the molecular conformation[44] by manually counting the number of chain crossovers per molecule n and by measuring superhelix pitch angles α using the angle measure tool in SPIP.

Analysis of movies recorded by high-speed AFM was performed using in-house-developed software written in Python, to calculate the center of mass and the radius of gyration of supercoiled plasmids. To this end the following analysis steps were carried out for each frame individually: first the background was removed according to Otsu's thresholding.[66] Since not all parts of the plasmid were connected in several images, a Gaussian filter was applied afterward to connect the plasmid fragments. Then, all objects not connected to the central plasmid were removed. As a last step, another combination of Otsu's thresholding and a Gaussian filter was applied to remove background pixels at the edges of the plasmid. Finally, the radius of gyration and the position of the center of mass were calculated based on the measured height values of the remaining nonzero pixels.

The individual background-corrected images are imported in the SPIP software, where dynamic elements of branched supercoiled plasmids could be analyzed. In each image the lengths l_i of the plectoneme arms were quantified by measuring the volume fraction of each arm with respect to the total plasmid volume using the "particle analysis" toolbox. The interarm angle ϕ_i was quantified by connecting the center of the supercoil branch point with the first crossover in each arm. The plectoneme bending flexibility was quantified in terms of a 2D WLC model with bending persistence length A_{plect} by measuring the end−end distance r_i and length λ_i of superhelix axes using the polygon shape tool.

We quantify dynamics of molecular conformations by calculating the autocorrelation $c_X(t)$ of a conformational parameter X as $c_X(t) = \frac{\langle X(t)\, X(0)\rangle - \langle X^2\rangle}{\sigma_X^2}$ where the brackets "$\langle\rangle$" denote averages over all conformational trajectories, and σ_X^2 is the variance of X. We fitted $c_X(t)$ by an exponential decay of the form $c_X(t) \approx \exp(-t/\tau)$ with τ being the autocorrelation time.

All fitting procedures and plotting were performed using MATLAB version R2015a. Unless indicated otherwise, errors on fit parameters are 95% confidence intervals.

Bending Energy of a Plectonemic Supercoil. We follow the analytical approximation for the bending energy in a plectonemic supercoil as first proposed by Hearst and Hunt:[47]

$$\Delta G_{bend} = \kappa_{bend} L k_0 \left(\frac{1 - \sqrt{1 - 16\pi^2 R^2 \left(\Delta Wr/Lk_0\right)^2}}{4R^2} - 2\pi^2 \left(\Delta Wr/Lk_0\right)^2 \right)$$

where κ_{bend} is the bend rigidity of DNA and R the DNA radius.

ASSOCIATED CONTENT

Supporting Information

The Supporting Information is available free of charge on the ACS Publications website at DOI: 10.1021/acsnano.8b06994.

Supporting Figures S1−3; Supporting Table S1; (PDF)
Supplementary Movie 1 (AVI)

AUTHOR INFORMATION

Corresponding Authors

*E-mail: jan.lipfert@lmu.de.
*E-mail: steven.defeyter@kuleuven.be.
*E-mail: willem.vanderlinden@kuleuven.be.

ORCID

Jan Lipfert: 0000-0003-3613-7896
Steven De Feyter: 0000-0002-0909-9292
Willem Vanderlinden: 0000-0002-2900-8087

Author Contributions

Conceptualization, W.V.; investigation, W.V., T.B., H.D., S.K.; resources, T.B., J.L., S.D., T.A., N.K.; original draft, W.V., T.B.;

DOI: 10.1021/acsnano.8b06994
ACS Nano 2018, 12, 11907−11916

funding acquisition, W.V., S.D., J.L., T.A.; supervision, W.V., SD., and J.L.

Notes

The authors declare no competing financial interest.
All data, materials, and custom-written Python software for data analysis are available upon reasonable request.

ACKNOWLEDGMENTS

We thank C. Broedersz, S. Granick, H. Gaub, M. Benoit, and W. Frederickx for discussions, A. Katan and K. Douglass for sharing the worm-like chain simulation code, K. Čermáková for help with protein purification, and Z. Debyser for use of laboratory equipment. We acknowledge funding from KU Leuven through an IDO grant and the Junior Mobility Programme (to T.B.), from the Deutsche Forschungsgemeinschaft through SFB 863 project A11, and from the Fonds Wetenschappelijk Onderzoek through a personal fellowship (to W.V.). H.D.K. acknowledges a Visiting Scientist position at Bio-AFM FRC, supported by a grant from the MEXT Japan (#15K21711 to T.A.).

REFERENCES

(1) Postow, L.; Hardy, C. D.; Arsuaga, J.; Cozzarelli, N. R. Topological Domain Structure of the Escherichia Coli Chromosome. *Genes Dev.* **2004**, *18*, 1766−1779.
(2) Naumova, N.; Imakaev, M.; Fudenberg, G.; Zhan, Y.; Lajoie, B. R.; Mirny, L. A.; Dekker, J. Organization of the Mitotic Chromosome. *Science* **2013**, *342*, 948−953.
(3) White, J. H. Self-Linking and the Gauss Integral in Higher Dimensions. *Am. J. Math.* **1969**, *91*, 693−728.
(4) Jeon, J.-H.; Adamcik, J.; Dietler, G.; Metzler, R. Supercoiling Induces Denaturation Bubbles in Circular DNA. *Phys. Rev. Lett.* **2010**, *105*, 208101.
(5) Lilley, D. M. The Inverted Repeat as a Recognizable Structural Feature in Supercoiled DNA Molecules. *Proc. Natl. Acad. Sci. U. S. A.* **1980**, *77*, 6468−6472.
(6) Rahmouni, A.; Wells, R. Stabilization of Z DNA *in Vivo* by Localized Supercoiling. *Science* **1989**, *246*, 358−363.
(7) Vanderlinden, W.; Lipfert, J.; Demeulemeester, J.; Debyser, Z.; De Feyter, S. Structure, Mechanics, and Binding Mode Heterogeneity of LEDGF/P75-DNA Nucleoprotein Complexes Revealed by Scanning Force Microscopy. *Nanoscale* **2014**, *6*, 4611−4619.
(8) Burns, H.; Minchin, S. Thermal Energy Requirement for Strand Separation during Transcription Initiation: The Effect of Supercoiling and Extended Protein DNA Contacts. *Nucleic Acids Res.* **1994**, *22*, 3840−3845.
(9) van den Broek, B.; Lomholt, M. A.; Kalisch, S.-M. J.; Metzler, R.; Wuite, G. J. L. How DNA Coiling Enhances Target Localization by Proteins. *Proc. Natl. Acad. Sci. U. S. A.* **2008**, *105*, 15738−15742.
(10) Finzi, L.; Dunlap, D. Supercoiling Biases the Formation of Loops Involved in Gene Regulation. *Biophys. Rev.* **2016**, *8*, 65−74.
(11) Bryant, Z.; Stone, M. D.; Gore, J.; Smith, S. B.; Cozzarelli, N. R.; Bustamante, C. Structural Transitions and Elasticity from Torque Measurements on DNA. *Nature* **2003**, *424*, 338.
(12) Strick, T. R.; Allemand, J. F.; Bensimon, D.; Bensimon, A.; Croquette, V. The Elasticity of a Single Supercoiled DNA Molecule. *Science* **1996**, *271*, 1835−1837.
(13) Brutzer, H.; Luzzietti, N.; Klaue, D.; Seidel, R. Energetics at the DNA Supercoiling Transition. *Biophys. J.* **2010**, *98*, 1267−1276.
(14) Kriegel, F.; Ermann, N.; Lipfert, J. Probing the Mechanical Properties, Conformational Changes, and Interactions of Nucleic Acids with Magnetic Tweezers. *J. Struct. Biol.* **2017**, *197*, 26−36.
(15) Walker, P. U.; Vanderlinden, W.; Lipfert, J. The Dynamics and Energy Landscape of DNA Plectoneme Nucleation. *bioRxiv* **2018**.
(16) Deufel, C.; Forth, S.; Simmons, C. R.; Dejgosha, S.; Wang, M. D. Nanofabricated Quartz Cylinders for Angular Trapping: DNA Supercoiling Torque Detection. *Nat. Methods* **2007**, *4*, 223.
(17) Forth, S.; Deufel, C.; Sheinin, M. Y.; Daniels, B.; Sethna, J. P.; Wang, M. D. Abrupt Buckling Transition Observed during the Plectoneme Formation of Individual DNA Molecules. *Phys. Rev. Lett.* **2008**, *100*, DOI: 10.1103/PhysRevLett.100.148301.
(18) van Loenhout, M. T. J.; de Grunt, M. V.; Dekker, C. Dynamics of DNA Supercoils. *Science* **2012**, *338*, 94−97.
(19) Ganji, M.; Kim, S. H.; van der Torre, J.; Abbondanzieri, E.; Dekker, C. Intercalation-Based Single-Molecule Fluorescence Assay To Study DNA Supercoil Dynamics. *Nano Lett.* **2016**, *16*, 4699−4707.
(20) Kim, S. H.; Ganji, M.; van der Torre, J.; Abbondanzieri, E.; Dekker, C. DNA Sequence Encodes the Position of DNA Supercoils. *bioRxiv* **2017**.
(21) Lyubchenko, Y. L.; Shlyakhtenko, L. S. Visualization of Supercoiled DNA with Atomic Force Microscopy *in Situ*. *Proc. Natl. Acad. Sci. U. S. A.* **1997**, *94*, 496−501.
(22) Bussiek, M.; Mücke, N.; Langowski, J. Polylysine-coated Mica Can Be Used to Observe Systematic Changes in the Supercoiled DNA Conformation by Scanning Force Microscopy in Solution. *Nucleic Acids Res.* **2003**, *31*, e137.
(23) Bustamante, C.; Vesenka, J.; Tang, C. L.; Rees, W.; Guthold, M.; Keller, R. Circular DNA Molecules Imaged in Air by Scanning Force Microscopy. *Biochemistry* **1992**, *31*, 22−26.
(24) van Noort, S. J. T.; van der Werf, K. O.; de Grooth, B. G.; Greve, J. High Speed Atomic Force Microscopy of Biomolecules by Image Tracking. *Biophys. J.* **1999**, *77*, 2295−2303.
(25) Tanigawa, M.; Okada, T. Atomic Force Microscopy of Supercoiled DNA Structure on Mica. *Anal. Chim. Acta* **1998**, *365*, 19−25.
(26) Schmatko, T.; Muller, P.; Maaloum, M. Surface Charge Effects on the 2D Conformation of Supercoiled DNA. *Soft Matter* **2014**, *10*, 2520−2529.
(27) Samorì, B.; Muzzalupo, I.; Zuccheri, G. Deposition of Supercoiled DNA on Mica for Scanning Force Microscopy Imaging. *Scanning Microsc.* **1996**, *10*, 952−953.
(28) Fuller, F. B. The Writhing Number of a Space Curve. *Proc. Natl. Acad. Sci. U. S. A.* **1971**, *68*, 815−819.
(29) Gore, J.; Bryant, Z.; Nöllmann, M.; Le, M. U.; Cozzarelli, N. R.; Bustamante, C. DNA Overwinds When Stretched. *Nature* **2006**, *442*, 836−839.
(30) Liebl, K.; Drsata, T.; Lankas, F.; Lipfert, J.; Zacharias, M. Explaining the Striking Difference in Twist-Stretch Coupling between DNA and RNA: A Comparative Molecular Dynamics Analysis. *Nucleic Acids Res.* **2015**, *43*, 10143−10156.
(31) Gross, P.; Laurens, N.; Oddershede, L. B.; Bockelmann, U.; Peterman, E. J. G.; Wuite, G. J. L. Quantifying How DNA Stretches, Melts and Changes Twist under Tension. *Nat. Phys.* **2011**, *7*, 731−736.
(32) Rivetti, C.; Guthold, M.; Bustamante, C. Scanning Force Microscopy of DNA Deposited onto Mica: Equilibration *versus* Kinetic Trapping Studied by Statistical Polymer Chain Analysis. *J. Mol. Biol.* **1996**, *264*, 919−932.
(33) Wiggins, P.; Van Der Heijden, T.; Moreno-Herrero, F.; Spakowitz, A.; Phillips, R.; Widom, J.; Dekker, C.; Nelson, P. C. High Flexibility of Dna on Short Length Scales Probed by Atomic Force Microscopy. *Nat. Nanotechnol.* **2006**, *1*, 137−141.
(34) Laurence, T. A.; Kong, X.; Jager, M.; Weiss, S. Probing Structural Heterogeneities and Fluctuations of Nucleic Acids and Denatured Proteins. *Proc. Natl. Acad. Sci. U. S. A.* **2005**, *102*, 17348−17353.
(35) Mathew-Fenn, R. S.; Das, R.; Harbury, P. A. B. Remeasuring the Double Helix. *Science* **2008**, *322*, 446−449.
(36) Zettl, T.; Mathew, R. S.; Seifert, S.; Doniach, S.; Harbury, P. A. B.; Lipfert, J. Absolute Intramolecular Distance Measurements with Angstrom-Resolution Using Anomalous Small-Angle X-Ray Scattering. *Nano Lett.* **2016**, *16*, 5353−5357.

DOI: 10.1021/acsnano.8b06994
ACS Nano 2018, 12, 11907−11916

(37) Baumann, C. G.; Smith, S. B.; Bloomfield, V. A.; Bustamante, C. Ionic Effects on the Elasticity of Single DNA Molecules. *Proc. Natl. Acad. Sci. U. S. A.* **1997**, *94*, 6185−6190.
(38) Abels, J. A.; Moreno-Herrero, F.; Van Der Heijden, T.; Dekker, C.; Dekker, N. H. Single-Molecule Measurements of the Persistence Length of Double-Stranded RNA. *Biophys. J.* **2005**, *88*, 2737−2744.
(39) Murugesapillai, D.; Bouaziz, S.; Maher, L. J.; Israeloff, N. E.; Cameron, C. E.; Williams, M. C. Accurate Nanoscale Flexibility Measurement of DNA and DNA-Protein Complexes by Atomic Force Microscopy in Liquid. *Nanoscale* **2017**, *9*, 11327−11337.
(40) Eeftens, J. M.; Katan, A. J.; Kschonsak, M.; Hassler, M.; de Wilde, L.; Dief, E. M.; Haering, C. H.; Dekker, C. Condensin Smc2-Smc4 Dimers Are Flexible and Dynamic. *Cell Rep.* **2016**, *14*, 1813−1818.
(41) Bettotti, P.; Visone, V.; Lunelli, L.; Perugino, G.; Ciaramella, M.; Valenti, A. Structure and Properties of DNA Molecules Over The Full Range of Biologically Relevant Supercoiling States. *Sci. Rep.* **2018**, *8*, 6163.
(42) Barth, M. C.; Dederich, D. A.; Dedon, P. C. An Improved Method for Large-Scale Preparation of Negatively and Positively Supercoiled Plasmid DNA. *BioTechniques* **2009**, *47*, 633−635.
(43) Keller, W. Determination of the Number of Superhelical Turns in Simian Virus 40 DNA by Gel Electrophoresis. *Proc. Natl. Acad. Sci. U. S. A.* **1975**, *72*, 4876−4880.
(44) Boles, T. C.; White, J. H.; Cozzarelli, N. R. Structure of Plectonemically Supercoiled DNA. *J. Mol. Biol.* **1990**, *213*, 931−951.
(45) Vologodskii, A. V.; Levene, S. D.; Klenin, K. V.; Frank-Kamenetskii, M.; Cozzarelli, N. R. Conformational and Thermodynamic Properties of Supercoiled DNA. *J. Mol. Biol.* **1992**, *227*, 1224−1243.
(46) Fathizadeh, A.; Schiessel, H.; Ejtehadi, M. R. Molecular Dynamics Simulation of Supercoiled DNA Rings. *Macromolecules* **2015**, *48*, 164−172.
(47) Hearst, J. E.; Hunt, N. G. Statistical Mechanical Theory for the Plectonemic DNA Supercoil. *J. Chem. Phys.* **1991**, *95*, 9322−9328.
(48) Tanigawa, M.; Okada, T. Atomic Force Microscopy of Supercoiled DNA Structure on Mica. *Anal. Chim. Acta* **1998**, *365*, 19−25.
(49) Landau, L. D.; Lifshitz, E. M. Theory of Elasticity. *Course of Theoretical Physics* **1986**, *3*, 195.
(50) Schlick, T.; Li, B.; Olson, W. K. The Influence of Salt on the Structure and Energetics of Supercoiled DNA. *Biophys. J.* **1994**, *67*, 2146−2166.
(51) Gennes, P.-G. *Scaling Concepts in Polymer Physics*; Cornell University Press, 1979.
(52) Lipfert, J.; Kerssemakers, J. W. J.; Jager, T.; Dekker, N. H. Magnetic Torque Tweezers: Measuring Torsional Stiffness in DNA and RecA-DNA Filaments. *Nat. Methods* **2010**, *7*, 977.
(53) Moroz, J. D.; Nelson, P. Torsional Directed Walks, Entropic Elasticity, and DNA Twist Stiffness. *Proc. Natl. Acad. Sci. U. S. A.* **1997**, *94*, 14418−14422.
(54) Nomidis, S. K.; Kriegel, F.; Vanderlinden, W.; Lipfert, J.; Carlon, E. Twist-Bend Coupling and the Torsional Response of Double-Stranded DNA. *Phys. Rev. Lett.* **2017**, *118*. DOI: 10.1103/PhysRevLett.118.217801
(55) Sheinin, M. Y.; Forth, S.; Marko, J. F.; Wang, M. D. Underwound DNA under Tension: Structure, Elasticity, and Sequence-Dependent Behaviors. *Phys. Rev. Lett.* **2011**, *107*, 108102.
(56) Ando, T.; Uchihashi, T.; Scheuring, S. Filming Biomolecular Processes by High-Speed Atomic Force Microscopy. *Chem. Rev.* **2014**, *114*, 3120−3188.
(57) Xu, Q.; Feng, L.; Sha, R.; Seeman, N. C.; Chaikin, P. M. Subdiffusion of a Sticky Particle on a Surface. *Phys. Rev. Lett.* **2011**, *106*, 228102.
(58) Daoud, M.; Joanny, J. F. Conformation of Branched Polymers. *J. Phys. (Paris)* **1981**, *42*, 1359−1371.
(59) Marko, J. F.; Siggia, E. D. Fluctuations and Supercoiling of DNA. *Science* **1994**, *265*, 506−508.
(60) Jia, D.; Muthukumar, M. Topologically Frustrated Dynamics of Crowded Charged Macromolecules in Charged Hydrogels. *Nat. Commun.* **2018**, *9*, 1−12.
(61) Maier, B.; Rädler, J. O. Conformation and Self-Diffusion of Single Dna Molecules Confined to Two Dimensions. *Phys. Rev. Lett.* **1999**, *82*, 1911−1914.
(62) Maier, B.; Rädler, J. O. DNA on Fluid Membranes: A Model Polymer in Two Dimensions. *Macromolecules* **2000**, *33*, 7185−7194.
(63) Langowski, J.; Kremer, W.; Kapp, U. Dynamic Light Scattering for Study of Solution Conformation and Dynamics of Superhelical DNA. *Methods Enzymol.* **1992**, *211*, 430−448.
(64) Jian, H.; Schlick, T.; Vologodskii, A. Internal Motion of Supercoiled DNA: Brownian Dynamics Simulations of Site Juxtaposition. *J. Mol. Biol.* **1998**, *284*, 287−296.
(65) Uchihashi, T.; Kodera, N.; Ando, T. Guide to Video Recording of Structure Dynamics and Dynamic Processes of Proteins by High-Speed Atomic Force Microscopy. *Nat. Protoc.* **2012**, *7*, 1193−1206.
(66) Otsu, N. Threshold Selection Method from Gray Level Histograms. *IEEE Trans. Syst. Man. Cybern.* **1979**, *9*, 62−66.

DOI: 10.1021/acsnano.8b06994
ACS Nano 2018, 12, 11907−11916